ACS APPLIED ENERGY MATERIALS

www.acsaem.org Article

Moisture-Driven Formation and Growth of Quasi-2-D Organolead Halide Perovskite Crystallites

Bryan R. Wygant, Geoff T. Geberth, Alexandre Z. Ye, Andrei Dolocan, Daniel E. Cotton, Sean T. Roberts, David A. Vanden Bout, and C. Buddie Mullins*

Cite This: https://dx.doi.org/10.1021/acsaem.0c00423 Read Online

ACCESS | Metrics & More | Article Recommendations | Supporting Information

ABSTRACT: Ruddlesden–Popper phase quasi-2-D organolead halide perovskites like *n*-butylammonium methylammonium lead iodide (*n*BA-MAPI) exhibit improved moisture stability over typical 3-D perovskite materials, making them exciting for use in a variety of applications such as photovoltaic (PV) devices. This improved stability is the result of a unique disproportionation-based degradation mechanism that protects the bulk of the *n*BA-MAPI from extensive damage through the formation of a protective, low-*n* surface layer. In addition to this surface layer, *n*BA-MAPI films also exhibit the dynamic growth of micrometer-scale crystallites and cracks at the surface of the film, unique and potentially important byproducts of quasi-2-D perovskite disproportionation. Here, we present a detailed study of these crystallites using several analytical techniques including photoluminescence spectroscopy (PL), confocal fluorescence microscopy (CFM), atomic force microscopy (AFM) combined with time-of-flight-secondary ion mass spectrometry (ToF-SIMS), and others in an effort to better understand the relationship between material disproportionation and crystallite growth. Our results show that the crystallites form after exposure to humid air and confirm that they are composed of low-*n* phases of *n*BA-MAPI. The crystallites are found to extend into the interior of the film and exhibit continued growth while exposed to moisture over 72 h. This growth is accompanied by both a decrease in the bulk 2-D phase and an increase in a 3-D-like phase in the surface PL spectra, indicating that the crystallites are likely a product of moisture-driven disproportionation. Importantly, similar crystallites are also observed to form within model PV devices, indicating that such processes must be accounted for when designing future devices containing materials like *n*BA-MAPI.

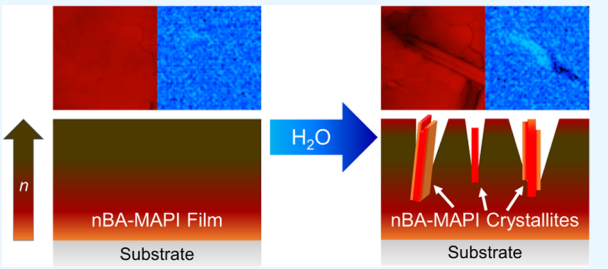

KEYWORDS: *perovskite, Ruddlesden–Popper phase, stability, moisture, crystal growth, degradation*

INTRODUCTION

In recent years, researchers have made a concerted effort to explore novel thin-film photovoltaic (PV) materials to augment solar energy production. Of the materials studied, organolead halide perovskites have been among the most promising to date, currently showing lab-scale device efficiencies that are near to that of polycrystalline Si devices.[1] The term perovskite is generally used to refer to any crystalline material with a stoichiometric composition of ABX_3, where A is typically an organic 1+ cation, B is a metallic 2+ cation, and X is a halide. The perovskites demonstrate a remarkable tolerance toward crystalline disorder and chemical impurities and can be synthesized using a variety of different precursors.[2] Methylammonium lead triiodide (MAPI) is generally regarded as the archetypical perovskite material, but the most efficient devices to date are typically composed of complex mixtures of different organic and inorganic A-site cations including formamidinium,[3] cesium,[4] guanidinium,[5] and rubidium,[6] as well as mixtures of iodide and bromide.[7] This flexibility allows for careful tuning and optimization of the electronic properties like the band gap and the conductivity of the material.[3]

A relatively recent innovation in the field has been the introduction of Ruddlesden–Popper phase organolead halide perovskites, with a generic stoichiometry of $A'_2A_{n-1}B_nX_{3n+1}$. Here, the A′ species is typically an amphiphilic alkylammonium species, such as *n*-butylammonium (*n*BA), that causes the ABX_3 crystal lattice to segregate into distinct quasi-2-D sheets.[8] These sheets are composed of PbI_6^{4-} octahedra and an A-site cation (Figure 1) and can range from sheets one octahedron thick to potentially over 7.[9] Below, we will be using the term *n* phase to refer to a material containing sheets of perovskite composed of *n* adjacent octahedra. While the thin sheets of the perovskite cause quantum confinement effects, which lead to wider band gaps and less light absorption than the more common 3-D perovskites,[10] researchers have shown

Received: February 27, 2020
Accepted: June 2, 2020
Published: June 2, 2020

https://dx.doi.org/10.1021/acsaem.0c00423
ACS Appl. Energy Mater. XXXX, XXX, XXX–XXX

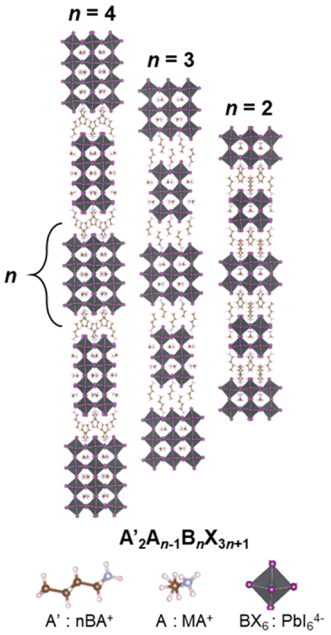

Figure 1. Crystal structures of the Ruddlesden–Popper phase perovskites sharing a chemical formula of $A'_2A_{n-1}B_nX_{3n+1}$, where n = 2, 3, and 4. Here, A′ is *n*-butylammonium, A is methylammonium, B is Pb, and X is iodide.

that these materials are considerably more stable when exposed to humidity than the related 3-D materials.[11−16] Thus, these quasi-2-D perovskites represent an interesting path to creating perovskite devices that are more resistant to the effects of moisture.

Work from our group and others has shown that this moisture resistance stems from a unique disproportionation-based degradation mechanism that helps to create a passivating layer of low-n (n = 1−3) species at the surface of a higher-n (n = 4+) material, inhibiting further degradation.[11,17] Briefly, upon exposure to moisture, the higher-n quasi-2-D organolead halide materials near the surface of the thin film partially decompose into an $(n - 1)$ phase and one equivalent of 3-D MAPI. This process is expected to be driven by the larger formation energy, and thus stability, of the lower-n phases as compared to the initial material.[18] Interestingly, we also observed the previously unreported formation of small crystallites at or near the surface of *n*-butylammonium methylammonium lead iodide (*n*BA-MAPI) films, which, indirect measurements using wide-angle X-ray scattering (WAXS) suggested, were composed of low-n perovskite.[17] While a thin, continuous, and conformal layer of such low-n perovskite is useful as a passivation layer to protect the perovskite from further damage,[19] these crystals are relatively thick, discrete, and oriented perpendicular to the plane of the film. As such they may in fact be deleterious, inducing damage and strain in the surrounding film as they grow and causing undesired changes to the band structure of the perovskite film. Given that these crystals arose simply from the exposure of an *n*BA-MAPI film to a humid environment and that such exposure may occur naturally during typical use of the perovskite devices, it is important to definitively identify and carefully study these crystals so that we can develop techniques to inhibit their formation.

To that end, we have used a suite of characterization techniques including X-ray diffraction spectroscopy (XRD), WAXS, atomic force microscopy (AFM), photoluminescence spectroscopy (PL), confocal fluorescence microscopy (CFM), and time-of-flight-secondary ion mass spectrometry (ToF-SIMS) to study the formation and growth of these crystallites on the surface of an *n*BA-MAPI film. XRD and WAXS measurements confirm that the fresh films exhibit excellent crystallinity and orientation relative to the substrate, while also showing that a low-n polycrystalline material forms in these films after 48 h of exposure to 78% relative humidity (RH). This corresponds to a similar increase in low-n and 3-D-like species in the PL spectra and a concurrent decrease in the n > 5 phase native to the film surface; together this is evidence of degradation by disproportionation. As such, in this work, we have adapted this previously presented quasi-2-D organolead halide degradation mechanism to better explain the range of chemical and physical changes that these materials undergo during exposure to moisture. Likewise, AFM images of an *n*BA-MAPI film exposed to humidity over 72 h show the appearance and growth of platelet-like structures at the surface of the film, which CFM spectra confirm to be composed of low-n phases. Finally, we used a combination of ToF-SIMS and AFM to study the topography of the interiors of both bare *n*BA-MAPI films and model PV devices exposed to moisture and discover evidence of these crystallites forming deep within the *n*BA-MAPI layer of each. Based on these results, we propose a mechanism to describe the crystal growth and perovskite disproportionation which occur in these films. Altogether, we provide a holistic view of the composition and formation of these crystals that will serve as a foundation for future attempts to mitigate, or even encourage, similar growth in new perovskite materials.

EXPERIMENTAL SECTION

Film Fabrication and Moisture Exposure. The *n*BA-MAPI films were fabricated using a hot casting method manner similar to our previous procedure.[17] Briefly, solutions of *n*-butylammonium iodide (*n*BAI, GreatCell Solar), methylammonium iodide (MAI, GreatCell Solar), and PbI_2 (99.99%, Alfa Aesar) in *N*,*N*-dimethylformamide (DMF, 99% ultra-dry, Acros Organics) were prepared in a N_2-filled glovebox (VAC Atmospheres, H_2O, O_2 < 5 ppm) by stirring for at least 24 h prior to film fabrication. The solutions were 0.5 M with respect to Pb^{2+} in solution, with a solution stoichiometry of $(nBA)_2(MA)_3Pb_4I_{13}$. Clean 2 × 2 cm^2 F:SnO_2 (FTO)-coated glass substrates (TEC15, Harford Glass) were washed in 1% (m/m) Contrex AP solution through sonication for 15 min and then lightly scrubbed and rinsed to remove any grease or debris. This was followed by 5 min of sonication in acetone and then 5 min more in isopropanol, before being dried with compressed air. After drying, the substrates were brought into the glovebox.

Prior to film deposition, an aliquot of perovskite precursor solution (typically 300−800 μL) was filtered through a 0.2 μm PTFE filter into a 2 mL glass vial and heated on a 75 °C hotplate for at least 20 min. Likewise, the FTO substrates were allowed to heat on a 110 °C hotplate for at least 20 min to ensure thorough heating as part of the hot casting procedure. Following heating, the substrate was rapidly moved to the chuck of a spin coater, where 80 μL of the preheated solution was pipetted onto the center of the film. The substrate was then immediately ramped to 5000 rpm and held for 20 s. Within 5 s, the substrate turned a dark brown color as the perovskite film crystallized. After spin coating, the film was removed from the chuck and allowed to continue cooling. The films were typically prepared as close to the time of experimentation as possible and stored out of direct light to inhibit photodegradation. To controllably degrade the films under humid conditions, they were placed in a sealed container containing a saturated solution of KCl in water, which kept the atmosphere inside the container at a relative humidity of 78%, for a

https://dx.doi.org/10.1021/acsaem.0c00423
ACS Appl. Energy Mater. XXXX, XXX, XXX−XXX

predetermined period of time. After degradation, the films were removed from the container and analyzed as quickly as possible.

Model PV devices for ToF-SIMS/AFM analysis were prepared similarly to above, with several additions. After drying, the FTO substrates were treated with UV/O_3 (BioForce Nanosciences) for 25 min to create a hydrophilic surface, and then, a PEDOT:PSS (Heraeus) film was applied to the surface. A 1:2 dilution of the polymer in methanol (Fisher Scientific, ACS Grade) was used for spin coating. Two drops of the PEDOT:PSS solution were filtered through a 0.2 μm PTFE filter onto the center of the substrate, which was then spun at 4000 rpm for 40 s, using a 3 s ramp and deceleration. Following coating, the substrates were annealed at 150 °C for 10 min before being immediately brought into the glovebox. Perovskite film deposition onto these substrates was accomplished in a manner identical to the procedure listed above.

To complete the model devices, 40 nm of C_{60} (MER Corp., 99.9%) and 7 nm of bathocuproine (BCP, Sigma-Aldrich, 99.9%) were thermally evaporated using an AMOD thermal evaporator at a base pressure of approximately 8×10^{-7} torr. The first 10 nm of C_{60} was deposited at a rate of 0.2 Å/s, while the remaining 30 nm was deposited at 1 Å/s; the 7 nm BCP film was deposited at 0.2 Å/s. Following deposition, thin strips of the BCP/C_{60}/perovskite/PEDOT:PSS stack was scratched away with a razor blade from two sides of the device to expose the FTO beneath. Gold (125 nm) was then deposited through a shadow mask via electron beam evaporation using a Cooke Evaporation System to create the top contacts (0.2 cm^2), as well as gold contacts for the FTO bottom contact to reduce unnecessary series resistance. Similar to C_{60}, the first 10 nm of Au was deposited at 0.2 Å/s and the remaining 115 nm was deposited at 1 Å/s. The finished devices were then stored in an Ar-filled MBraun glovebox (O_2/H_2O < 0.1 ppm) until testing.

Instrumental Characterization. X-ray diffraction (XRD) was performed on a Rigaku Ultima IV diffractometer in a thin-film configuration using a Cu Kα X-ray source. Atomic force microscopy (AFM) was conducted on a Park NX10 atomic force microscope in noncontact mode. This microscope was enclosed in a climate-controlled box allowing a constant RH to be maintained during analysis. The box was purged with ultra-high-purity N_2 gas for 1 h prior to sample loading to reduce the humidity to <15% before the fresh films were analyzed, and then, the humidity was increased to 78% for film exposure. For the ToF-SIMS/AFM measurements, the AFM box was purged continuously with ultra-high-purity N_2 gas, which kept the RH level very low to minimize the reaction between residual water and the Cs-sputtered spots. Photoluminescence spectroscopy (PL) was performed on a Horiba Jobin Yvon Fluorolog3 spectrophotometer, using an excitation wavelength of 450 nm and a typical 90° detector geometry, with the film held at 45°. Excitation was performed on both the front (shining directly on the perovskite film) and the back (shining through the glass) of the films. Wide-angle X-ray scattering (WAXS) was performed on a Xenocs Ganesha small-angle scattering instrument fitted with a moveable Dectris 300k detector to record wide-angle scattering data. The instrument is fitted with a microfocus Cu Kα source operated at 50 kV and 0.6 mA. A manufacturer-supplied utility, SAXSGUI, was used to reduce the 2-D scattering intensity images into intensity vs scattering angle plots. Data was collected from a 0.7×12 mm^2 area, using a 1° tilt of the substrate. Scanning electron microscopy (SEM) was performed with an FEI Quanta 650 ESEM, using an accelerating voltage of 15 kV at a vacuum of approximately 5×10^{-6} torr.

In preparation for the confocal fluorescence microscopy (CFM) studies, the perovskite films were placed face-up on fresh piranha solution-cleaned coverslips in a custom-machined sample holder that held them together with a secure contact. The fluorescence microscopy was performed with a custom-built microscope in a confocal scheme with 488 nm excitation and a 100× oil objective (Zeiss) in a Zeiss Axiovert 200 inverted microscope. Due to the highly emissive nature of the samples and the sensitivity of the detectors, the excitation power was too low to be measured. The piezo stage was controlled through a home-written Labview program (National Instruments). The emitted light was filtered through a 496 nm long-pass filter and a 721 nm short-pass filter and was directed onto either an APD (Perkin Elmer) or a spectrograph (Princeton Instruments, Acton SP-150) that was coupled with a liquid N_2-cooled CCD detector for imaging and spectroscopy, respectively. Each crystallite had spectra taken at three positions, once on each end and once in the middle. Each spot on a given crystal had three consecutive spectra taken with 25 s integration times. These three spectra were then averaged to increase the signal-to-noise ratio.

Time-of-flight-secondary ion mass spectrometry (ToF-SIMS) depth profiling in negative polarity was performed using a Bi_3^+ (30 keV ion energy, 0.8 pA measured sample current) analysis beam to raster scan a 100×100 μm^2 area located within the boundaries of a larger crater (300×300 μm^2) created using a Cs^+ sputtering beam (500 eV ion energy, ~40 nA measured sample current). The pressure inside the analysis chamber was typically below 1.5×10^{-9} torr during analysis. Both the films and devices analyzed using ToF-SIMS were split into half inside the glovebox prior to analysis, with one half left inside the glovebox as a control and the other half exposed to humidity. After exposure, the device or film was brought back into the glovebox and loaded with the control into an inert atmosphere transfer vessel to limit exposure to the environment while transferring the devices to and from the ToF-SIMS instrument. Following sputtering, the samples were loaded back into the vessel and transferred back to a glovebox to prepare them for AFM analysis. The samples were transferred under the inert atmosphere into the AFM box (<15% RH) and analyzed quickly to prevent any physical and chemical interactions of water or oxygen with residual Cs in the sputtered areas.

RESULTS AND DISCUSSION

XRD Analysis. We used the *n*BA-MAPI films with a nominal $n = 4$ stoichiometry similar to those previously reported in the literature[13,17] to more closely investigate film degradation and crystal growth in humid environments, fabricated using a hot casting method previously shown to produce well-oriented *n*BA-MAPI films.[13] The proper crystallographic orientation of the quasi-2-D perovskite is important in devices made using these materials, as it allows for charge conduction within the planes of the perovskite and thus improves the device efficiency.[20] The XRD spectrum of a freshly fabricated film (Figure S1) shows only two sharp peaks near 2θ = 14.2 and 28.5° (Figure 2a), in agreement with previous reports on the nominally $n = 4$ *n*BA-MAPI films. Frequently, polycrystalline 2-D organolead halide perovskite powders and unoriented films show peaks in the region below $2\theta = 10°$,[21] but our unexposed film shows no peaks here (Figure 2b), indicating a well-oriented film. WAXS measurements of the film prior to exposure (Figure S2a) further confirm this, with the WAXS spectra exhibiting distinct Bragg diffraction spots, which correspond to the primary crystallographic planes of the *n*BA-MAPI material oriented perpendicular to the substrate.[13,14]

After confirming the crystallographic uniformity and orientation of the films, we repeated both the XRD and WAXS measurements after 6, 12, 24, 48, and 72 h of exposure to a 78% RH environment to study what changes occur. The full XRD spectra of the films did not show significant changes to the relative intensity of the two primary peaks (Figure S1), only a slight 0.1−0.3° shift of the major peaks following exposure (Figure 1a). Such a shift could be due to an expansion of the perovskite unit cell due to humidity-induced hydration, but we believe that it is more likely the result of a slight increase in the relative quantity of lower-*n* perovskite species, which exhibit (111) and (202) peaks at slightly smaller 2θ than our initial material.[21] Previous studies have shown that

https://dx.doi.org/10.1021/acsaem.0c00423
ACS Appl. Energy Mater. XXXX, XXX, XXX−XXX

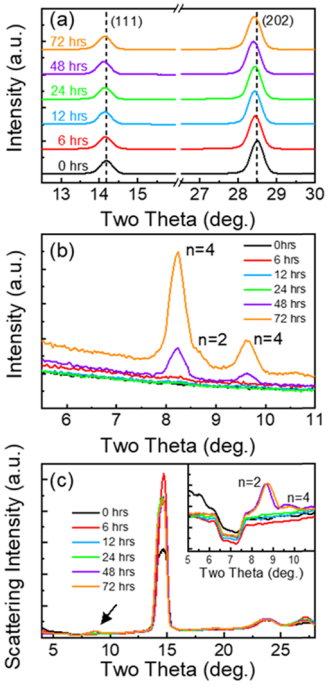

Figure 2. (a) Selected regions of the XRD spectrum of the *n*BA-MAPI film over 72 h of exposure to 78% RH, showing a shift in the (111) and (202) peaks. (b) Low two theta region of the *n*BA-MAPI film XRD spectrum over 72 h of humidity exposure, showing the formation of $n = 2$ and 4 phases in the film. (c) Radial integrations of the WAXS spectra of the *n*BA-MAPI film over 72 h of exposure, showing variations in the peak intensity of the main peak, in addition to the formation of $n = 2$ and 4 peaks (inset).

the *n*BA-MAPI films composed of multiple n phases exhibit XRD spectra with a single (111) and (202) peak, which is likely a composite of the peaks for the various n phases present in the film.[22] Because of the composite nature of this peak, an increase in the quantity of low-n species present would therefore shift the position of the peak to lower angles. More interestingly, after 48 h of exposure, we observe the appearance of two peaks at $2\theta = 8.2$ and 9.7° and index these to the $n = 4$ phase; the two peaks grow stronger after 72 h and are joined by an additional $n = 2$ peak at $2\theta = 8.65°$.[21] Likewise, the WAXS spectra for the films exposed for 48 and 72 h show the formation of two Debye−Scherrer diffraction rings at low q values (indicated by the white arrows in Figure S2e,f), and radial integration of the spectra confirms that these peaks correspond to the $2\theta = 8.65$ and 9.7° peaks visible in the XRD spectra (Figure 2c).[21] Such rings are typically indicative of unoriented crystals in the film,[23] and their appearance is suggestive of the formation of low-n crystals in the film as a result of moisture-driven disproportionation.[17]

AFM Analysis of the Film Surface. To better study the morphology and growth of the crystals indicated by the ring patterns in the WAXS spectra, we conducted AFM analysis of the *n*BA-MAPI film surface during different stages of moisture exposure. Using a microscope inside of a sealed container, we monitored the degradation of a film *in situ* over the course of 3 days. The initial AFM images of the surface show that the initial film surface is very smooth, with a root-mean-squared (RMS) roughness of only 5 nm (Figures 3a and S3a). However, after 6 h (Figure 3b) of exposure, the film begins to show the formation of extended micron-long cracks (location I) and small pits (location II), which extend into the bulk of the film, as well as several nodules extending above the surface. AFM shows that the cracks extend roughly 10−40 nm into the film surface, but the sharp edges of the cracks and their relatively narrow width may prevent the AFM tip from accurately reading their true depth.

The time-lapse images of a single area of the film (Figures 3 and S3) show that the density of the cracks at the surface continues to increase with exposure to moisture. Notably, between 12 and 24 h, we observe the formation of the thin, elongated crystallites within the cracks themselves (Figure 3c, location I). On average, these crystallites appear to be roughly 2−3 μm long and approximately 100 nm wide. The crystallites exhibit flat faces perpendicular to their narrow edges, indicating that the crystallites may be quasi-2-D platelets, which extend into the film rather than the 1-D rods laying

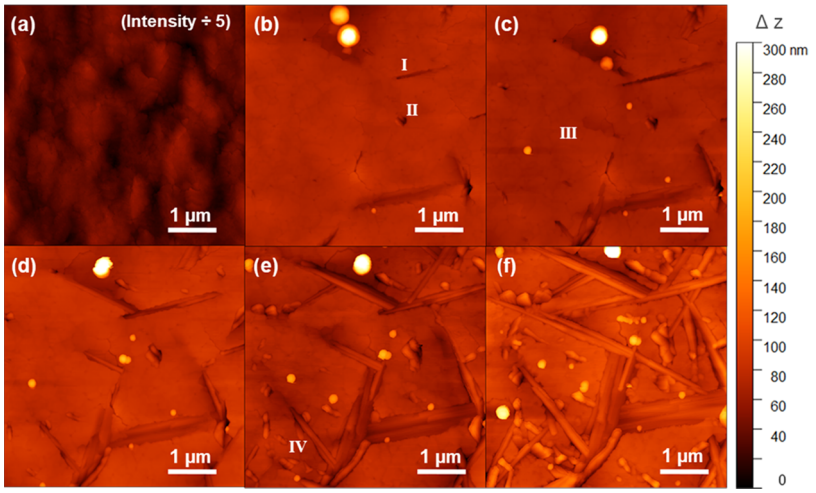

Figure 3. AFM images of a single area of the *n*BA-MAPI film in noncontact mode after (a) 0, (b) 6, (c) 12, (d) 24, (e) 48, and (f) 72 h of exposure to 78% RH. (a) shows that the film is initially smooth (RMS 5 nm) with only small ridges and valleys at the surface of the film, but upon extended exposure to humidity, cracks (location I) and holes (location II) begin to form, with the elongated crystals forming later. Some grain boundaries also experience subsidence (location III) prior to crystal growth, and other areas exhibit crystal growth without apparent damage to the film previously (location IV).

https://dx.doi.org/10.1021/acsaem.0c00423
ACS Appl. Energy Mater. XXXX, XXX, XXX−XXX

within the cracks themselves. Similar microscale crystallites have previously been reported on perovskite films treated to create an artificial 2-D perovskite layer, as well as in the 2-D films exposed to humidity for extended periods of time.[17,24] Given their random orientation in the film and that the Ruddlesden−Popper phase organolead halide perovskites are well known to adopt similar stacked platelet structures upon crystallization in solution,[25] these crystallites seem to correspond to the low-*n* perovskite previously evidenced by the XRD and WAXS spectra.

These crystallites continue to grow over the course of 72 h of observation as new gaps and crystals also emerge, resulting in a rough surface covered in both the features. (Figure 3f). Because the measurements were made *in situ*, we can more closely study the process by which the crystals appear to grow and relate these observations to previous work in solution-based systems. As previously noted, the crystals appear to grow out of cracks in the perovskite that formed as the film was exposed to humidity. Interestingly most, if not all, of these cracks appear to form at the grain boundaries between the individual *n*BA-MAPI grains, which compose the film. Over time, the crystals grow in thickness and appear to force these cracks wider, separating previously adjacent crystal grains on the surface (location I). Given that these boundaries are likely the weakest points in the film and where it is most permeable to humidity, these are unsurprising but important observations.

We also observe evidence of apparent subsidence along the grain boundaries in the film, most notably near the very center of Figure 3b,c (location III). Between 6 and 12 h, several grains on one side of a grain boundary dropped sharply downward into the film, and after 24 h, Figure 3d shows that a crystal formed at this location. This appears to be evidence of some form of the dynamic process deeper in the film, which directly impacts the stability of the surface and which is related to the appearance and growth of the crystals. In addition to the formation of the long, thin cracks, we also observed holes that appeared to be more or less round, with several examples visible in Figures 3 and S3b. The crystals emerge from these holes after continued exposure to moisture, similar in appearance to those growing from the cracks but generally smaller and shorter overall (Figure 3d, location II). Similar short crystals appear to be able to form without the initial hole, as is visible in the bottom left corner of Figure 3f (location IV), suggesting that there may be at least two distinct crystal growth pathways available in these films.

After the first appearance, the crystals grew primarily in length rather than in thickness, likely along the plane of the quasi-2-D sheets. This growth appears to be limited primarily by the presence of other crystals in the path of growth, based on the observations of the crystals in Figure 3d. Almost all of the crystals also appear to increase in thickness and height with time, although at a much slower rate than that of growth along the long axis. Most of the crystals appear to initially measure approximately 90 nm wide but grow to an average thickness of 150 nm after 72 h. Additionally, many of the crystals appeared to grow and develop into two distinct, adjacent platelets as exposure continues, giving them a layered appearance that is not dissimilar to the macroscopic images of the 2-D perovskites.[11] From the images, it is not clear if the two crystals grow and develop separately or if the second grows as part of the development of the first. Finally, with regard to vertical growth, we observe that the crystals initially appeared to be recessed into the film and slowly grew toward the surface until they were either level with or very slightly above the average level of the film; this may indicate that their growth is limited by the availability of the material from the bulk film surrounding them. Taken together, these AFM results provide a detailed look at how the films physically change with exposure to moisture, as well as the types of structural evolutions that the *n*BA-MAPI crystals undergo during formation and growth. Unfortunately, the AFM results are unable to differentiate between the different *n* phases indicated in the XRD and WAXS results, preventing a definitive assignment of which *n* phases compose these crystals.

Bulk Photoluminescence Spectroscopy. To further study which low-*n* phases form during moisture exposure and crystal growth, we also conducted PL analysis of the *n*BA-MAPI films during degradation. Previous reports using this technique have reported the presence of multiple *n* phases from a nominally $n = 4$ film, the result of an inherent gradient in the *n* phases comprising the film as a function of depth.[26,27] Due to an increase in the thermodynamic stability of the *n*BA-MAPI phases as *n* decreases, the hot cast *n*BA-MAPI solutions tend to form films that feature low-*n* phases at the FTO interface and very high-*n* phases, similar to 3-D MAPI, near the surface.[27] Recently, Liu et al. provided a much clearer *n* phase depth map of the hot cast *n*BA-MAPI films and showed that for the relatively thick (∼1 μm) films, there are three distinct regions of *n* phase composition within the film.[28] The top third of their film is almost completely composed of a high-*n* ($n > 5$) species, while the bottom third is dominated by $n = 3$ and 4 species, with shoulders corresponding to $n = 2$ and 5. The middle portion appears to be a transition zone, where the high- and low-*n* species are both present in various quantities.

While we are unable to probe the center of our film directly, the PL spectra taken from the front and back of our films (Figure 4a) show a similar peak distribution to those previously reported.[17,28] As a result, we find it very likely that our films exhibit a similar *n* phase distribution to that of Liu et al., illustrated in Figure 4c. The front-side spectrum shows a broad peak centered near 715 nm with an asymmetric shoulder toward shorter wavelengths, and we note that the peak is shifted to shorter wavelengths than the peak reported by Liu et al. We suggest that this may be due to the relative thinness of our films (∼350 nm, Figure S4), inhibiting the formation of a large $n\text{BA}^+$ concentration gradient during fabrication and thus creating a less 3-D-like surface.[27] The back-side spectra of our film show a broad distribution of peaks ranging from 575 to 715 nm, previously identified as the $n = 2-5$ peaks of *n*BA-MAPI.[21]

After confirming the composition of the unexposed *n*BA-MAPI films, we exposed the material to a 78% RH environment over 72 h in a similar manner to the film analyzed by XRD and recorded the PL spectra from both the front and back sides at various time points. Similar to our previous report,[17] we observe the formation of low-*n* peaks at the surface of the film after just 6 h of exposure, which become more distinct as additional time passes (Figure S5a). Small changes are observed in the back-side spectra (Figure S5b), including a slight shift in the $n = 3$ peak to longer wavelength, indicating crystallographic changes as the perovskite interacts with moisture. Likewise, the primary front-side peak shifts by 10−725 nm after 72 h of exposure, a result of the formation of higher-*n* species during degradation and disproportionation of the perovskite under humid conditions. This is clearly evidenced by the difference plot of the front- and back-side

https://dx.doi.org/10.1021/acsaem.0c00423
ACS Appl. Energy Mater. XXXX, XXX, XXX−XXX

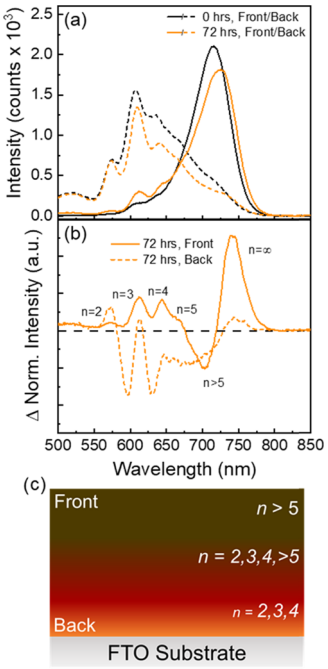

Figure 4. (a) PL spectra of the front (solid) and back (dashed) sides of the *n*BA-MAPI film, before and after 72 h of exposure to 78% RH. After 72 h, the intensity of both the spectra decreases, and the peaks between 575 and 650 nm appear on the front. (b) Difference spectra of the normalized PL spectra from the front and back of a film after 72 h of exposure, showing the formation of low-*n* and 3-D-like species and a concurrent decrease of the $n > 5$ peak due to disproportionation. (c) Graphic representing the proposed *n* phase structure of the *n*BA-MAPI film.

spectra after 72 h (Figure 4b), where, in addition to the aforementioned growth of the $n = 2-5$ species, the front-side spectrum also shows clear growth of a peak near 740 nm assigned to a 3-D-like perovskite in the previous reports.[28] This peak is visible in both the front- and back-side spectra recorded at all exposure times (Figure S5c,d) and is accompanied by a loss of the $n > 5$ peak. Taken together, the growth of low- and high-*n* species at the expense of the original *n*BA-MAPI material during exposure to moisture indicates that the films are likely undergoing disproportionation as they degrade in humid environments.

These observations agree well with the similar changes in the XRD and WAXS spectra and, based on the polycrystalline nature of these newly formed phases as determined by the ring patterns in the WAXS spectra, further confirm that the crystals we observe growing in the AFM images are composed of these low-*n* phases. Like the film in which they are embedded, the surfaces of these crystals are also likely to undergo disproportionation into progressively lower-*n* phases, resulting in a surface of $n = 1-3$ surrounding a core of $n = 4$ and larger phases.[10,29] The local quantum well-like band structure resulting from this *n* phase arrangement is expected to trap electrons photogenerated within the crystallites at the crystallite surfaces. This will prevent charge transfer from the crystallites to the $n > 5$ film surrounding them and allow the $n = 1-5$ phases in the crystallites to be visible in the PL spectra; a more detailed explanation is presented in our previous work.[17] This hypothesis is supported by recent work showing similar low-*n* 2-D surface features in Pb−Sn perovskite films visible with hyperspectral PL mapping.[30] Unfortunately, while the strong correlation between the XRD, WAXS, AFM, and PL data allows us to infer the *n* phases contained in the crystals, none of these techniques allow for direct identification, and a more precise technique is thus required to do so.

Fluorescence Microscopy Analysis. Confocal fluorescence microscopy (CFM) is one such technique and offers both the spatial and spectral resolution necessary to accurately probe and confirm the *n* phase composition of the small crystallites in these films. CFM is regularly used to measure the fluorescence of both single molecules and molecular aggregates,[31−33] and using this technique, we can generate both total fluorescence images of the film surface and point fluorescence spectra from single diffraction-limited spots on the film. Together, these capabilities make it ideal for both imaging the crystals visible by AFM and identifying their composition. A point spectrum from the unexposed *n*BA-MAPI film shows a single intense fluorescence peak near 740 nm (Figure S6), which is significantly red-shifted from the primary peak in the bulk PL spectrum (Figure 4a). Similar in PL wavelength to the species observed by Liu et al., it is evidence of a thin surface layer of 3-D-like perovskite.[28] Due to the intensity of the peak, we used a 721 nm short-pass filter for further imaging and spectroscopy, which allowed us to focus more closely on the region of the PL spectra occupied by low-*n* perovskite phases.

Prior to moisture exposure, the CFM images of the *n*BA-MAPI films with the short-pass filter in place show no evidence of crystals at the surface (Figure S7a), in agreement with the AFM images. Following 12 h of exposure, however, we begin to observe elongated regions of fluorescence in the CFM images that increase in intensity and surface density over the course of 72 h of exposure (Figure S7b−e). Additionally, high-resolution CFM imaging of a film exposed for 24 h (Figure 5a) shows that the regions (such as the example circled in white)

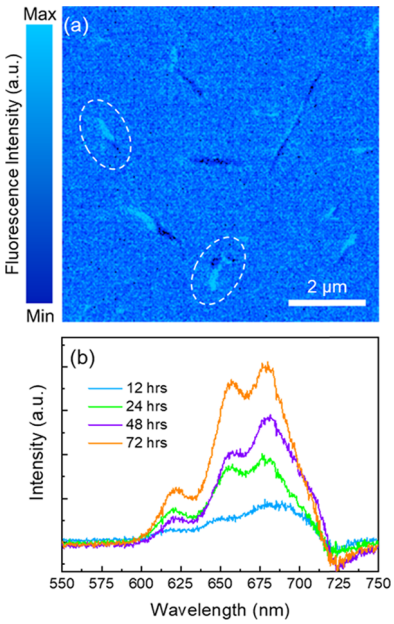

Figure 5. (a) CFM image of the *n*BA-MAPI film exposed to 78% RH for 24 h, showing localized fluorescence below 740 nm from crystal-like structures, such as the circled examples. (b) Average background-corrected point fluorescence spectra from the low-*n* *n*BA-MAPI crystals after moisture exposure for 72 h, showing an increase in the intensity of $n = 3-5$ peaks with increasing exposure to humidity.

https://dx.doi.org/10.1021/acsaem.0c00423
ACS Appl. Energy Mater. XXXX, XXX, XXX−XXX

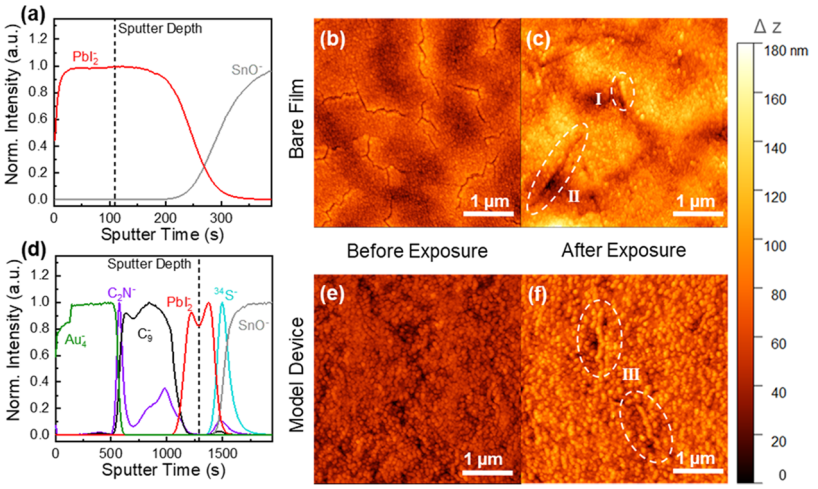

Figure 6. Negative ion polarity ToF-SIMS depth profiles for (a) bare *n*BA-MAPI film and (d) model PV device. PbI_2^- represents the inorganic portion of the perovskite, CN^- represents the organic portion of the perovskite, SnO^- represents FTO, Au_4^- represents the Au contact, C_2N^- represents BCP, C_9^- represents the C_{60} layer, and $^{34}S^-$ represents the PEDOT:PSS layer. A fresh film (b) and one exposed to 78% RH for 8 h (c) were sputtered to the dashed line in (a) and the surface was imaged by AFM, showing the presence of new crystals (I) and cracks (II) only in the interior of the exposed sample. A fresh device (e) and one exposed to humidity for 24 h (f) likewise showing the formation of crystals (III) inside the film.

are roughly 1 μm long and 100 nm wide, as well as dark areas that appear identical to the surface cracks visible in the AFM images. Taken together, the CFM images are strong evidence that these regions correspond to the crystals previously observed using AFM.

After using CFM imaging to locate the low-*n* crystals, we used the point spectra taken from the crystals and films at each exposure condition to study how the *n* phase composition of the crystals changed with time. To do so, we measured point spectra from both off- and on-crystal sites and generated average spectra of each type of site (Figure S8). This allowed us to create background-subtracted on-crystal spectra at each time point between 12 and 72 h (Figure 5b). These spectra show that as exposure continues, the crystals exhibit progressively stronger signals for peaks corresponding to n = 3−5 phases, indicating an increase in the abundance of these phases as the crystals grow. We note that these CFM peaks exhibit a 10 nm red shift when compared to the bulk PL spectra (i.e., n = 3 at 610 nm in PL but 620 nm in CFM), which is evidence of crystal compression due to the surrounding film.[34] In all, the phases and changes we observe in the CFM agree with the bulk PL measurements and confirm that the low-*n* features we observe in the bulk spectra come from these smaller crystallites.

In addition to measuring the average spectra from multiple crystals, we also analyzed the point spectra taken from three separate points on individual crystals (the middle and both ends) and compared them to determine the relative compositional homogeneity of the individual crystals as a function of exposure time. Examples are provided in Figure S9, and we find that the homogeneity of the crystals decreases significantly over time (Figure S9c), a reflection of the rough and uneven surface observed with AFM. As a result of this roughness and the resolution of the microscope (~200 nm) due to the incident laser when compared to the crystal width, we are currently unable to provide a more quantitative analysis of the spatial composition of the crystallites. Despite this, our CFM images and spectra not only confirm that the crystals visible via AFM are composed of n = 3−5 *n*BA-MAPI phases, but also that no significant phase changes occur on the rest of the film surface during film degradation. This does not preclude the presence of other phases at the surface, either as a result of an initially disordered material[29] or as a function of disproportionation,[17] but it does indicate that if they exist they are likely transferring charge to other, higher-*n* phases and would not be expected to negatively impact charge conduction in a full device.

ToF-SIMS/AFM. As mentioned above, Liu et al. recently showed that the surface 3-D-like perovskite phase in a hot cast *n*BA-MAPI thin film extended roughly a third of the way into the film before gradually giving way to low-*n* phases. Given that the AFM images during moisture exposure appear to show cracks into the film forming prior to crystal growth, we used a combination of time-of-flight-secondary ion mass spectrometry (ToF-SIMS) and AFM to study the topography of the interior of our films before and after degradation and determine if the crystals might form within the film rather than at the surface. Similar to previous reports on both 2-D materials[35] and organic solar cells,[36] ToF-SIMS allowed us to controllably sputter to the interior of the film before imaging and analyzing the topography of the freshly uncovered surface using AFM.

Figure 6a shows the full depth profile of the *n*BA-MAPI film acquired in negative ion polarity, with PbI_2^- representing the inorganic portion of the perovskite and SnO^- representing the FTO substrate. We next sputtered approximately 50% of the way through the film (approximately 175 nm), as indicated by the dashed line in Figure 6a, using the ToF-SIMS before removing the film from the instrument and subsequently analyzing the surface using AFM. The uniform ion sputtering from the ToF-SIMS preserves the ridge and valley pattern previously visible on the surface in Figure 3a, as well as some of the grain boundaries between individual *n*BA-MAPI crystallites (Figure 6b). In addition, the exposed surface is uniformly covered in small nodules that are likely artifacts of ion sputtering. Figure 6c shows that after sputtering through a film exposed to moisture for 8 h, several 1−2 μm long cracks are visible in the newly exposed surface of the film (location II); these are similar in appearance to those visible in Figure 3c and

https://dx.doi.org/10.1021/acsaem.0c00423
ACS Appl. Energy Mater. XXXX, XXX, XXX−XXX

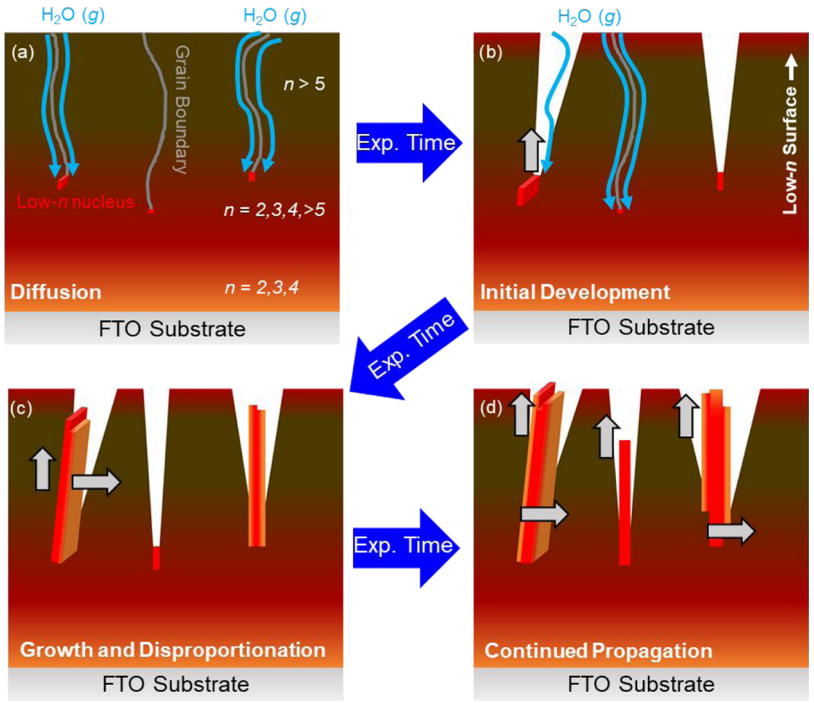

Figure 7. Proposed growth mechanism for low-*n* *n*BA-MAPI crystallites. (a) Water diffuses through grain boundaries in the $n > 5$ surface, carrying solvated perovskite components to low-*n* nuclei buried in the bulk of the film. The nuclei begin to grow in height and length, causing the film above them to split (b) and allowing more water to diffuse into the film. As exposure continues (c), the crystals also begin to exhibit growth in thickness, as well as disproportionation. These processes continue (d), with the crystals eventually ceasing vertical growth near the film surface but continuing to lengthen and widen as exposure continues.

indicate that the cracks at the surface extend deeply into the film. Additionally, a few linear structures, likely the bases of the crystals seen at the surface of the film, were also visible near some of the cracks (location I). Their presence in the center of the film shows that the crystals visible at the surface also extend into the interior of the film, and may even originate there, while their proximity to the cracks further suggests a link between the two features.

In light of these observations, as well as the importance of perovskite stability in photovoltaic devices, we next fabricated model device stacks and analyzed them using a similar ToF-SIMS/AFM experiment to investigate how the presence of C_{60} and Au overlayers might affect the formation of these crystallites. Selected ionic species in the ToF-SIMS depth profile of the device (Figure 6d) show the presence of the various components of the device: Au_4^- for the Au contact, C_2N^- for the bathocuproine, C_9^- for the C_{60} electron-transport material, PbI_2^- for the *n*BA-MAPI, $^{34}S^-$ for the PEDOT:PSS hole-transport material, and SnO^- for the FTO substrate. After sputtering to the center of the *n*BA-MAPI layer of a fresh device, also indicated by the dashed line in the depth profile, we observe a similar interior morphology to that of the fresh bare film (Figure 6e). Once again, the surface is relatively featureless and covered with small nodules, with no other extended structures visible. This is to be expected given the pristine nature of the device and indicates that there are few differences that arise in the AFM image of the interior of the *n*BA-MAPI as a result of sputtering through the Au and C_{60} overlayers.

Next, based on previous reports of 2-D device stability,[13,17] we exposed our devices to 24 h of humidity exposure to induce a moderate degree of damage to the device before once again sputtering to the center of the *n*BA-MAPI layer and imaging it with AFM. Figure 6f shows a mostly level surface largely dominated by the small sputtering-induced nodules. Unlike the fresh sample, however, the interior of the degraded device does appear to show additional features. Near the center of Figure 6f (location III) is a roughly 1 μm long, 100 nm wide structure, with a second similar structure slightly below it. These distinct structures are similar in appearance to those observed in the interior of the degraded film (Figure 6c, location I), as well as the low-*n* crystals visible at the surface in Figure 3. The surface density of these structures is much lower than was observed in even the 6 h film in Figure 3b, likely a result of decreased water diffusion through the overlayers. Additionally, no clear cracks in the film are visible near them, which may be the result of increased film rigidity due to the presence of the C_{60} layer above.

The increased strength and moisture protection offered by the overlayers seem to inhibit the growth of the low-*n* crystallites we observe in the bare films, but Figure 6f suggests that it does not halt the process completely. Indeed, identical devices have shown a relatively gradual decrease in their power conversion efficiency (PCE) during the same time period, before exhibiting significant performance loss only 12 h later. We hypothesize that this relatively rapid loss of PCE could be due to the delayed growth of low-*n* crystals within the *n*BA-MAPI layer causing chemical and structural damage like that observed at earlier times in bare films. Further work is necessary to fully explore this proposal, but the evidence of crystal growth within full devices we present here suggests that quasi-2-D crystal growth should be taken into account when developing the devices based on the Ruddlesden–Popper phase perovskites.

Proposed Crystal Growth Mechanism. Drawing upon the data presented above, we have developed a proposed

https://dx.doi.org/10.1021/acsaem.0c00423
ACS Appl. Energy Mater. XXXX, XXX, XXX−XXX

process by which the crystallographic and morphologic changes we observe in our *n*BA-MAPI films occur (Figure 7). To begin, while the presence of Bragg spots in our WAXS data indicates that our films are well oriented and crystalline, the breadth of the peaks, particularly the $(\bar{1}1\bar{1})$ peak, indicates a moderate degree of disorder in the films. Qiu et al. have reported similarly broad peaks in the grazing-incidence WAXS (GIWAXS) spectra of Sn-based *n*BA-containing perovskites, which they attribute to the formation of intermediate low-*n* 2-D phases during film fabrication.[37] While they are able to suppress the formation of these phases through addition of a second spacer species (phenylethylammonium), without this addition, the films show increased disorder in the orientation of the predominant perovskite phases. This has also been seen in some Pb-based 2-D perovskites.[14] In addition to this crystallographic disorder, our films also contain a gradient *n* phase composition from top to bottom, with *n* increasing with film thickness. Combined with the moisture-driven disproportionation, we believe that these features explain the crystal formation and growth we observe.

As water diffuses through the more permeable grain boundaries at the film surface, likely slowed by the hydrophobic $n\text{BA}^+$ tails,[19] it eventually penetrates through the high-*n* surface layer and into the mixed-phase region below (Figure 7a). Based on the native disorder in the films, we propose that the mixed region contains segregated areas of $n = 3-5$, either in the form of small discontinuities in the crystal lattice or as small grains of low-*n* material within the bulk. Evidence of similar segregated phases has been observed in related systems,[38] supporting this hypothesis. These crystallites would act as local low-*n* nucleation sites within the bulk of the film, where solvated perovskite compounds dissolved as the water diffused through the high-*n* layer above could recrystallize. DFT calculations have shown that the low-*n* phases are more stable, providing a thermodynamic driving force for this dissolution and recrystallization.[18] Further, given that the alkylammonium components are more likely to be solvated than the Pb−I lattice, this process may also explain the disproportionation observed previously, simultaneously creating new low-*n* species in the bulk and higher-*n* species at the surface, evidenced by the peak shift observed in Figure S5a. Some of the solvated species may also recrystallize at the film surface, resulting in the passivation layer previously hypothesized to exist there.[11,17] The lack of clear polycrystallinity in the WAXS is evidence that these nuclei are oriented such that the 2-D sheets are perpendicular to the substrate. Thus, the crystals would exhibit preferential edge-on growth along the edge of the quasi-2-D sheets,[39] resulting in characteristic platelet-like crystals of Ruddlesden−Popper materials.[25] As they grow, the grain boundaries above will split open (Figure 7b), creating the cracks we observe in the AFM images (Figure 3).

With cracks opening in the surface, the film becomes more permeable to moisture, accelerating the vertical growth of the nascent crystals at the bottom of the cracks. This growth would further split the cracks, exposing new high-*n* *n*BA-MAPI along the walls to moisture and inducing strain on the film. This strain may allow diffusion through the previously unfavorable grain boundaries, allowing new nuclei to grow and opening more cracks (Figure 7c). The crystals would grow vertically until water is no longer able to efficiently diffuse solvated species to the leading crystal growth edge, explaining the limited vertical growth observed by AFM. In turn, this would encourage additional growth on the flat faces and edges of the platelets, widening and lengthening the crystals and the cracks. Compression of the crystals' lattices due to the surrounding film could cause a decrease in the perovskite band gap, explaining the red-shifted spectra in Figure S8b. The CFM spectra of the crystals themselves show that they contain $n = 3-5$ phases. Higher-$n = 4$ and 5 phases would be expected to disproportionate into lower-*n* phases with time as well, potentially indicated by the increased crystal point spectra heterogeneity indicated in Figure S9c.

This process of water diffusion to buried nuclei followed by crystal growth and disproportionation would continue as long as the film was exposed to humidity (Figure 7d), resulting in the dynamic surface covered in cracks and crystals we observe in our bare films. Such films represent a "best-case" scenario for degradation, however, as it allows for minimal protection of the films as they are exposed to water. Even still, the AFM image in Figure 6f indicates that despite the protective overlayers, the *n*BA-MAPI layers of the full devices appear to undergo a similar process, albeit more slowly. This slower rate may be due in part to the surface disproportionation previously described by our group in full devices,[17] as the formation of a lower-*n* surface at the C_{60}/*n*BA-MAPI interface would likely stabilize the surface and inhibit the diffusion of soluble nuclei in the bulk. Formation of this lower-*n* surface is evidenced by a widening of the PbI_2^- peak in the ToF-SIMS experiments after moisture exposure (Figure S10), as it occurred primarily in the hydration region present at the C_{60}/*n*BA-MAPI interface. A similar perovskite widening was previously observed in the films that had suffered moisture damage.

To better relate the physical and chemical changes observed here with the changes in the performance of the PV devices, we have included the results from a degradation study of the identical *n*BA-MAPI devices exposed to 78% RH conditions (Figures S11 and S12).[17] During exposure, the devices appeared to undergo a multistep degradation process, with two distinct degradation phases separated by a plateau in PCE loss from approximately 12 to 24 h (Figure S12a). Our ToF-SIMS/AFM results may provide an explanation for the two-step loss of PV performance observed in these devices. In the first step (0−12 h), surface disproportionation occurs at the C_{60}/*n*BA-MAPI interface, resulting in a negligible loss of the performance as a protective low-*n* layer forms that protects the bulk of the film. Gradually, sufficient water diffuses through the film to induce nucleation of the crystals within the bulk, causing both physical and chemical damage to the device. This culminates in a second, more severe loss of performance beginning after 24 h of exposure. Given that this process is proposed to be dependent upon the presence of nuclei within the bulk of the film, techniques that increase the homogeneity of similar films throughout their depth may be an effective way to prevent or inhibit the crystal growth. Recently, careful control of the substrate temperature during film fabrication[28] and the addition of a second linker species[37] have been shown to have some control over the distribution of phases in the film, making them promising avenues for future work. Experiments are currently underway to investigate this further, including the use of FIB milling to generate cross sections of devices at different levels of exposure, which can then be analyzed using TEM and other high-resolution techniques.

https://dx.doi.org/10.1021/acsaem.0c00423
ACS Appl. Energy Mater. XXXX, XXX, XXX−XXX

CONCLUSIONS

In the present work, we have used a series of spectroscopic and microscopy techniques to explore the composition, morphology, and growth of previously unstudied crystals forming on the surface of the *n*BA-MAPI films. The XRD and WAXS spectra of the fresh samples confirm that the films are oriented largely perpendicular to the underlying substrate and are highly crystalline. After exposure to humidity, the films exhibit the growth of polycrystalline low-*n* phases over time, confirmed by AFM to be platelet-like structures buried in the film, roughly 2−3 μm in length and 100 nm in width. The PL spectra taken at identical exposure times likewise show increases in low-*n* species, as well as the growth of 3-D-like peaks in the difference spectra; this is concurrent with a decrease in the $n > 5$ 2-D species and indicative of perovskite disproportionation. The CFM images and spectra confirm that the crystals visible in the AFM images are composed of these newly formed, low-*n* phases, consistent with the WAXS spectra. Using ToF-SIMS/AFM, we have shown that the crystal features visible at the film surface extend deep into the bulk and that similar crystallites are also visible in the AFM images taken from the interior of the model *n*BA-MAPI perovskite devices. This suggests that a similar process of degradation also occurs in the active layers of full 2-D organolead halide solar devices. Using our combined data, we propose a mechanism to explain the crystal growth during water exposure, which accounts for the developments we observe. Together, our results suggest that future research should pursue thin-film fabrication methods that limit heterogeneity within the quasi-2-D perovskite films. We expect this to prevent the creation of the low-*n* nuclei in the bulk that allow for crystal growth and thus film damage, which in turn should lead to improved device lifetimes.

ASSOCIATED CONTENT

Supporting Information

The Supporting Information is available free of charge at https://pubs.acs.org/doi/10.1021/acsaem.0c00423.

> Full XRD spectra of the films exposed to 78% RH, WAXS spectra of the films over 72 h of moisture exposure, additional AFM images, cross-sectional SEM image of the film, full PL spectra and normalized difference plots, unfiltered CFM spectra, CFM images over 72 h of moisture exposure, CFM spectra on and off of the crystallites, *n*BA-MAPI device PV performance and the degradation results (PDF)

AUTHOR INFORMATION

Corresponding Author

C. Buddie Mullins − *Department of Chemistry, McKetta Department of Chemical Engineering, and Texas Material Institute, University of Texas at Austin, Austin, Texas 78712, United States;* orcid.org/0000-0003-1030-4801; Email: mullins@che.utexas.edu

Authors

Bryan R. Wygant − *Department of Chemistry, University of Texas at Austin, Austin, Texas 78712, United States*

Geoff T. Geberth − *Department of Chemistry, University of Texas at Austin, Austin, Texas 78712, United States*

Alexandre Z. Ye − *McKetta Department of Chemical Engineering, University of Texas at Austin, Austin, Texas 78712, United States*

Andrei Dolocan − *Texas Material Institute, University of Texas at Austin, Austin, Texas 78712, United States;* orcid.org/0000-0001-5653-0439

Daniel E. Cotton − *Department of Chemistry, University of Texas at Austin, Austin, Texas 78712, United States*

Sean T. Roberts − *Department of Chemistry, University of Texas at Austin, Austin, Texas 78712, United States;* orcid.org/0000-0002-3322-3687

David A. Vanden Bout − *Department of Chemistry, University of Texas at Austin, Austin, Texas 78712, United States*

Complete contact information is available at: https://pubs.acs.org/10.1021/acsaem.0c00423

Notes

The authors declare no competing financial interest.

ACKNOWLEDGMENTS

The authors gratefully acknowledge the support of the Robert A. Welch Foundation via grant F-1436 as well as the United States Department of Energy, Basic Energy Sciences via grant no. DE-FG02-09ER16119. S.T.R. and D.E.C. acknowledge the support from the National Science Foundation CAREER award (CHE-1654404) as well as the Robert A. Welch Foundation via grant F-1885. D.E.C. also thanks the Texas Materials Institute for providing access to instrumentation for WAXS.

REFERENCES

(1) NREL. Best Research-Cell Efficiencies. https://www.nrel.gov/pv/assets/pdfs/pv-efficiency-chart.20181221.pdf.

(2) Kim, H. S.; Hagfeldt, A.; Park, N. G. Morphological and Compositional Progress in Halide Perovskite Solar Cells. *Chem. Commun.* **2019**, *55*, 1192−1200.

(3) Prochowicz, D.; Runjhun, R.; Tavakoli, M. M.; Yadav, P.; Saski, M.; Alanazi, A. Q.; Kubicki, D. J.; Kaszkur, Z.; Zakeeruddin, S. M.; Lewiński, J.; Grätzel, M. Engineering of Perovskite Materials Based on Formamidinium and Cesium Hybridization for High-Efficiency Solar Cells. *Chem. Mater.* **2019**, *31*, 1620−1627.

(4) Wang, H.; Bian, H.; Jin, Z.; Zhang, H.; Liang, L.; Wen, J.; Wang, Q.; Ding, L.; Liu, S. F. Cesium Lead Mixed-Halide Perovskites for Low-Energy Loss Solar Cells with Efficiency beyond 17%. *Chem. Mater.* **2019**, *31*, 6231−6238.

(5) Zhang, W.; Xiong, J.; Li, J.; Daoud, W. A. Guanidinium Induced Phase Separated Perovskite Layer for Efficient and Highly Stable Solar Cells. *J. Mater. Chem. A* **2019**, *7*, 9486−9496.

(6) Turren-Cruz, S. H.; Saliba, M.; Mayer, M. T.; Juárez-Santiesteban, H.; Mathew, X.; Nienhaus, L.; Tress, W.; Erodici, M. P.; Sher, M. J.; Bawendi, M. G.; Grätzel, M.; Abate, A.; Hagfeldt, A.; Correa-Baena, J. P. Enhanced Charge Carrier Mobility and Lifetime Suppress Hysteresis and Improve Efficiency in Planar Perovskite Solar Cells. *Energy Environ. Sci.* **2018**, *11*, 78−86.

(7) Gil-Escrig, L.; Momblona, C.; La-Placa, M. G.; Boix, P. P.; Sessolo, M.; Bolink, H. J. Vacuum Deposited Triple-Cation Mixed-Halide Perovskite Solar Cells. *Adv. Energy Mater.* **2018**, *8*, No. 1703506.

(8) Cao, D. H.; Stoumpos, C. C.; Farha, O. K.; Hupp, J. T.; Kanatzidis, M. G. Two-Dimensional Homologous Perovskites as Light Absorbing Materials for Solar Cell Applications. *J. Am. Chem. Soc.* **2015**, *137*, 7843−7850.

(9) Myae Soe, C. M.; Nagabhushana, G. P.; Shivaramaiah, R.; Tsai, H.; Nie, W.; Blancon, J. C.; Melkonyan, F.; Cao, D. H.; Traoré, B.; Pedesseau, L.; Kepenekian, M.; Katan, C.; Even, J.; Marks, T. J.; Navrotsky, A.; Mohite, A. D.; Stoumpos, C. C.; Kanatzidis, M. G. Structural and Thermodynamic Limits of Layer Thickness in 2D Halide Perovskites. *Proc. Natl. Acad. Sci. U.S.A.* **2019**, *116*, 58−66.

(10) Silver, S.; Dai, Q.; Li, H.; Brédas, J. L.; Kahn, A. Quantum Well Energetics of an n = 2 Ruddlesden−Popper Phase Perovskite. *Adv. Energy Mater.* **2019**, No. 1901005.
(11) Stoumpos, C. C.; Soe, C. M. M.; Tsai, H.; Nie, W.; Blancon, J. C.; Cao, D. H.; Liu, F.; Traoré, B.; Katan, C.; Even, J.; Mohite, A. D.; Kanatzidis, M. G. High Members of the 2D Ruddlesden-Popper Halide Perovskites: Synthesis, Optical Properties, and Solar Cells of (CH3(CH2)3NH3)2(CH3NH3)4Pb5I16. *Chem* **2017**, *2*, 427−440.
(12) Grancini, G.; Roldán-Carmona, C.; Zimmermann, I.; Mosconi, E.; Lee, X.; Martineau, D.; Narbey, S.; Oswald, F.; De Angelis, F.; Graetzel, M.; Nazeeruddin, M. K. One-Year Stable Perovskite Solar Cells by 2D/3D Interface Engineering. *Nat. Commun.* **2017**, *8*, No. 15684.
(13) Tsai, H.; Nie, W.; Blancon, J.-C.; Stoumpos, C. C.; Asadpour, R.; Harutyunyan, B.; Neukirch, A. J.; Verduzco, R.; Crochet, J. J.; Tretiak, S.; Pedesseau, L.; Even, J.; Alam, M. A.; Gupta, G.; Lou, J.; Ajayan, P. M.; Bedzyk, M. J.; Kanatzidis, M. G.; Mohite, A. D. High-Efficiency Two-Dimensional Ruddlesden−Popper Perovskite Solar Cells. *Nature* **2016**, *536*, 312−316.
(14) Wang, Z.; Lin, Q.; Chmiel, F. P.; Sakai, N.; Herz, L. M.; Snaith, H. J. Efficient Ambient-Air-Stable Solar Cells with 2D-3D Heterostructured Butylammonium-Caesium-Formamidinium Lead Halide Perovskites. *Nat. Energy* **2017**, *2*, No. 17135.
(15) Lee, J. W.; Dai, Z.; Han, T. H.; Choi, C.; Chang, S. Y.; Lee, S. J.; De Marco, N.; Zhao, H.; Sun, P.; Huang, Y.; Yang, Y. 2D Perovskite Stabilized Phase-Pure Formamidinium Perovskite Solar Cells. *Nat. Commun.* **2018**, *9*, No. 3021.
(16) Thote, A.; Jeon, I.; Lee, J. W.; Seo, S.; Lin, H. S.; Yang, Y.; Daiguji, H.; Maruyama, S.; Matsuo, Y. Stable and Reproducible 2D/3D Formamidinium-Lead-Iodide Perovskite Solar Cells. *ACS Appl. Energy Mater.* **2019**, *2*, 2486−2493.
(17) Wygant, B. R.; Ye, A. Z.; Dolocan, A.; Vu, Q.; Abbot, D. M.; Mullins, C. B. Probing the Degradation Chemistry and Enhanced Stability of 2D Organolead Halide Perovskites. *J. Am. Chem. Soc.* **2019**, *141*, 18170−18181.
(18) Quan, L. N.; Yuan, M.; Comin, R.; Voznyy, O.; Beauregard, E. M.; Hoogland, S.; Buin, A.; Kirmani, A. R.; Zhao, K.; Amassian, A.; Kim, D. H.; Sargent, E. H. Ligand-Stabilized Reduced-Dimensionality Perovskites. *J. Am. Chem. Soc.* **2016**, *138*, 2649−2655.
(19) Koh, T. M.; Shanmugam, V.; Guo, X.; Lim, S. S.; Filonik, O.; Herzig, E. M.; Müller-Buschbaum, P.; Swamy, V.; Chien, S. T.; Mhaisalkar, S. G.; Mathews, N. Enhancing Moisture Tolerance in Efficient Hybrid 3D/2D Perovskite Photovoltaics. *J. Mater. Chem. A* **2018**, *6*, 2122−2128.
(20) Chen, A. Z.; Shiu, M.; Ma, J. H.; Alpert, M. R.; Zhang, D.; Foley, B. J.; Smilgies, D. M.; Lee, S. H.; Choi, J. J. Origin of Vertical Orientation in Two-Dimensional Metal Halide Perovskites and Its Effect on Photovoltaic Performance. *Nat. Commun.* **2018**, *9*, No. 1336.
(21) Stoumpos, C. C.; Cao, D. H.; Clark, D. J.; Young, J.; Rondinelli, J. M.; Jang, J. I.; Hupp, J. T.; Kanatzidis, M. G. Ruddlesden-Popper Hybrid Lead Iodide Perovskite 2D Homologous Semiconductors. *Chem. Mater.* **2016**, *28*, 2852−2867.
(22) Zhou, N.; Shen, Y.; Li, L.; Tan, S.; Liu, N.; Zheng, G.; Chen, Q.; Zhou, H. Exploration of Crystallization Kinetics in Quasi Two-Dimensional Perovskite and High Performance Solar Cells. *J. Am. Chem. Soc.* **2018**, *140*, 459−465.
(23) Soe, C. M. M.; Nie, W.; Stoumpos, C. C.; Tsai, H.; Blancon, J. C.; Liu, F.; Even, J.; Marks, T. J.; Mohite, A. D.; Kanatzidis, M. G. Understanding Film Formation Morphology and Orientation in High Member 2D Ruddlesden−Popper Perovskites for High-Efficiency Solar Cells. *Adv. Energy Mater.* **2018**, *8*, No. 1700979.
(24) Li, L.; Zhou, N.; Chen, Q.; Shang, Q.; Zhang, Q.; Wang, X.; Zhou, H. Unraveling the Growth of Hierarchical Quasi-2D/3D Perovskite and Carrier Dynamics. *J. Phys. Chem. Lett.* **2018**, *9*, 1124−1132.
(25) Wang, K.; Wu, C.; Yang, D.; Jiang, Y.; Priya, S. Quasi-Two-Dimensional Halide Perovskite Single Crystal Photodetector. *ACS Nano* **2018**, *12*, 4919−4929.
(26) Liu, J.; Leng, J.; Wu, K.; Zhang, J.; Jin, S. Observation of Internal Photoinduced Electron and Hole Separation in Hybrid Two-Dimentional Perovskite Films. *J. Am. Chem. Soc.* **2017**, *139*, 1432−1435.
(27) Quintero-Bermudez, R.; Gold-Parker, A.; Proppe, A. H.; Munir, R.; Yang, Z.; Kelley, S. O.; Amassian, A.; Toney, M. F.; Sargent, E. H. Compositional and Orientational Control in Metal Halide Perovskites of Reduced Dimensionality. *Nat. Mater.* **2018**, *17*, 900−907.
(28) Liu, N.; Liu, P.; Ren, H.; Xie, H.; Zhou, N.; Gao, Y.; Li, Y.; Zhou, H.; Bai, Y.; Chen, Q. Probing Phase Distribution in 2D Perovskites for Efficient Device Design. *ACS Appl. Mater. Interfaces* **2020**, *12*, 3127−3133.
(29) Yuan, M.; Quan, L. N.; Comin, R.; Walters, G.; Sabatini, R.; Voznyy, O.; Hoogland, S.; Zhao, Y.; Beauregard, E. M.; Kanjanaboos, P.; Lu, Z.; Kim, D. H.; Sargent, E. H. Perovskite Energy Funnels for Efficient Light-Emitting Diodes. *Nat. Nanotechnol.* **2016**, *11*, 872−877.
(30) Ruggeri, E.; Anaya, M.; Gałkowski, K.; Delport, G.; Kosasih, F. U.; Abfalterer, A.; Mackowski, S.; Ducati, C.; Stranks, S. D. Controlling the Growth Kinetics and Optoelectronic Properties of 2D/3D Lead−Tin Perovskite Heterojunctions. *Adv. Mater.* **2019**, No. 1905247.
(31) Eisele, D. M.; Knoester, J.; Kirstein, S.; Rabe, J. P.; Vanden Bout, D. A. Uniform Exciton Fluorescence from Individual Molecular Nanotubes Immobilized on Solid Substrates. *Nat. Nanotechnol.* **2009**, *4*, 658−663.
(32) Elacqua, E.; Geberth, G. T.; Vanden Bout, D. A.; Weck, M. Synthesis and Folding Behaviour of Poly(p-Phenylene Vinylene)-Based β-Sheet Polychromophores. *Chem. Sci.* **2019**, *10*, 2144−2152.
(33) Hu, Z.; Shao, B.; Geberth, G. T.; Vanden Bout, D. A. Effects of Molecular Architecture on Morphology and Photophysics in Conjugated Polymers: From Single Molecules to Bulk. *Chem. Sci.* **2018**, *9*, 1101−1111.
(34) Postorino, P.; Malavasi, L. Pressure-Induced Effects in Organic-Inorganic Hybrid Perovskites. *J. Phys. Chem. Lett.* **2017**, *8*, 2613−2622.
(35) Chou, H.; Ismach, A.; Ghosh, R.; Ruoff, R. S.; Dolocan, A. Heterostructures at the Atomic Level. *Nat. Commun.* **2015**, *6*, No. 7482.
(36) Griffin, M. P.; Gearba, R.; Stevenson, K. J.; Vanden Bout, D. A.; Dolocan, A. Revealing the Chemistry and Morphology of Buried Donor/Acceptor Interfaces in Organic Photovoltaics. *J. Phys. Chem. Lett.* **2017**, *8*, 2764−2773.
(37) Qiu, J.; Xia, Y.; Zheng, Y.; Hui, W.; Gu, H.; Yuan, W.; Yu, H.; Chao, L.; Niu, T.; Yang, Y.; Gao, X.; Chen, Y.; Huang, W. 2D Intermediate Suppression for Efficient Ruddlesden-Popper (RP) Phase Lead-Free Perovskite Solar Cells. *ACS Energy Lett.* **2019**, *4*, 1513−1520.
(38) Lin, Y.; Fang, Y.; Zhao, J.; Shao, Y.; Stuard, S. J.; Nahid, M. M.; Ade, H.; Wang, Q.; Shield, J. E.; Zhou, N.; Moran, A. M.; Huang, J. Unveiling the Operation Mechanism of Layered Perovskite Solar Cells. *Nat. Commun.* **2019**, *10*, No. 1008.
(39) Riedinger, A.; Ott, F. D.; Mule, A.; Mazzotti, S.; Knüsel, P. N.; Kress, S. J. P.; Prins, F.; Erwin, S. C.; Norris, D. J. An Intrinsic Growth Instability in Isotropic Materials Leads to Quasi-Two-Dimensional Nanoplatelets. *Nat. Mater.* **2017**, *16*, 743−748.

https://dx.doi.org/10.1021/acsaem.0c00423
ACS Appl. Energy Mater. XXXX, XXX, XXX−XXX